

Light-evoked dendritic spikes in sustained but not transient rabbit retinal ganglion cells

Highlights

- Dendritic electrical excitability is cell-class-specific in rabbit retinal OFF-GCs
- Visual stimuli initiate dendritic spikes in sustained but not in transient OFF-GCs
- Dendritic spikes compute local motion in sustained OFF-GCs
- OFF-GC classes signal distinct aspects of an approaching predator

Authors

Arne Brombas, Xiangyu Zhou,
Stephen R. Williams

Correspondence

srw@uq.edu.au

In brief

Brombas et al. perform simultaneous electrical recordings from the soma and dendrites of rabbit OFF retinal ganglion cells to reveal that the differential expression of active dendritic integration defines cell-class-specific computations and the representation of moving visual stimuli.

Article

Light-evoked dendritic spikes in sustained but not transient rabbit retinal ganglion cells

Arne Brombas,¹ Xiangyu Zhou,¹ and Stephen R. Williams^{1,2,*}

¹Queensland Brain Institute, The University of Queensland, Brisbane, QLD 4072, Australia

²Lead contact

*Correspondence: srw@uq.edu.au

<https://doi.org/10.1016/j.neuron.2022.06.009>

SUMMARY

Dendritic computations have a central role in neuronal function, but it is unknown how cell-class heterogeneity of dendritic electrical excitability shapes physiologically engaged neuronal and circuit computations. To address this, we examined dendritic integration in closely related classes of retinal ganglion cells (GCs) using simultaneous somato-dendritic electrical recording techniques in a functionally intact circuit. Simultaneous recordings revealed sustained OFF-GCs generated powerful dendritic spikes in response to visual input that drove action potential firing. In contrast, the dendrites of transient OFF-GCs were passive and did not generate dendritic spikes. Dendritic spike generation allowed sustained, but not transient, OFF-GCs to signal into action potential output the local motion of visual stimuli to produce a continuous wave of action potential firing in adjacent cells as images moved across the retina. Conversely, this representation was highly fragmented in transient OFF-GCs. Thus, a heterogeneity of dendritic excitability defines the computations executed by classes of GCs.

INTRODUCTION

Active dendritic integration is thought to increase the computational capacity of neurons (London and Häusser, 2005; Stuart and Spruston, 2015). A mechanistic description of the role of active dendritic integration in neuronal circuit operations has, however, remained largely elusive. Although calcium imaging and electrophysiological recording have demonstrated the recruitment of active dendritic integration during forebrain circuit operations (Beaulieu-Laroche et al., 2019; Bittner et al., 2015; Doron et al., 2020; Lavzin et al., 2012; Moore et al., 2017; Rolotti et al., 2022; Schmidt-Hieber et al., 2017; Sheffield and Dombeck, 2015; Smith et al., 2013; Takahashi et al., 2016; Xu et al., 2012), relating the cell-class-specific role of dendritic information processing to function in complex forebrain circuits is challenging and hindered by the heterogeneity of dendritic integrative operations of anatomically and molecularly defined neuronal classes (Cembrowski and Spruston, 2019; Fletcher and Williams, 2019; Malik et al., 2016; Pastoll et al., 2020; Soltesz and Losonczy, 2018).

To circumvent these difficulties, the retina, a three-layered neuronal network, has emerged as an important model system to address the role of dendritic information processing in circuit computations. The retina executes defined neuronal computations to produce abstractions of the visual world, which are signaled to the higher brain by ~30 physiologically and anatomically defined classes of output neurons, termed retinal ganglion cells (GCs) (Baden et al., 2016; Sanes and Masland, 2015). This neuronal network can be maintained *ex vivo*, remains responsive

to physiological stimuli, and is amenable to high-resolution electrophysiological recordings. Leveraging on these advantages, previous work has mechanistically established that active dendritic integration has a central role in the computation of retinal direction selectivity (Brombas et al., 2017; Jain et al., 2020; Oesch et al., 2005; Sivyer and Williams, 2013; Trenholm et al., 2014), although the universality of this mechanism across the multiple classes of ON- and ON-OFF direction-selective GCs that sample visual space has been questioned (Poleg-Polsky and Diamond, 2016; Vaney et al., 2012). In contrast, the role of active dendritic integration in computations executed by other classes of retinal GCs has not been directly explored, and more generally, it is unknown if there is cell-class heterogeneity of the electrical excitability of retinal GC dendrites, other than that inferred, indirectly, from calcium imaging experiments (Ran et al., 2020). It should be noted that pioneering dendritic electrical recordings from enzymatically treated rabbit retinal preparations have demonstrated the variable initiation and forward propagation of dendritic spikes in retinal GCs (Velte and Masland, 1999). It remains unknown, however, if active dendritic integration is engaged by physiological stimuli in a GC class-specific manner.

Here, through the refinement of recording techniques (Brombas et al., 2017; Sivyer and Williams, 2013), we use simultaneous somatic and dendritic whole-cell recordings to explore the dendritic excitability of two related retinal GC classes, sustained and transient OFF-GCs that respond to dark visual stimuli, share molecular markers, and are distributed in close proximity across the retina (Sanes and Masland, 2015). Our results reveal

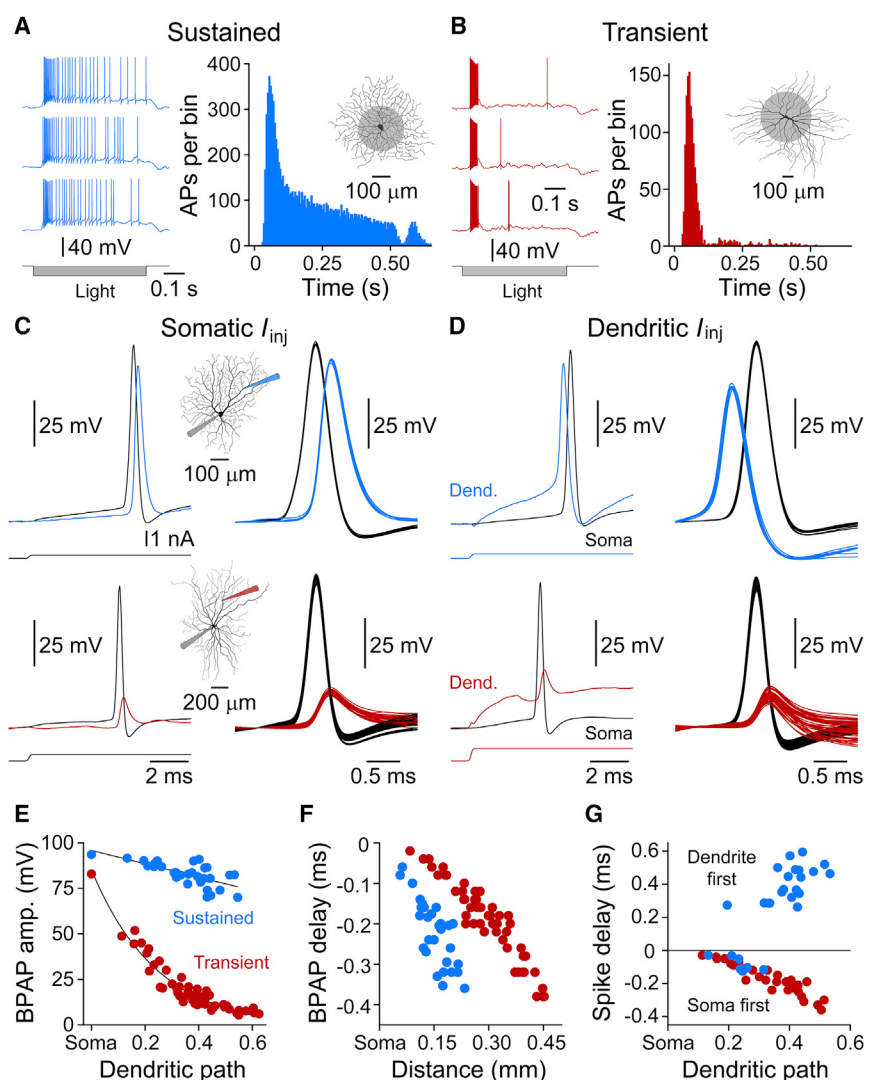


Figure 1. Cell-class-specific patterns of dendritic excitability

(A and B) AP firing patterns of a sOFF (A) and tOFF (B) GC in response to dark visual stimuli. The time course of visual stimuli are shown (Light). The graphs represent peristimulus time histograms of AP firing in sustained ($n = 46$) and transient ($n = 12$) OFF-GCs. Morphology and visual stimuli are inset. (C) Simultaneous somatic (black traces) and dendritic (colored traces) recording of APs in a sustained and transient OFF-GC evoked by threshold somatic current steps. Morphology and placement of recording electrodes are inset.

(D) Dendritic spikes are initiated in a sOFF but not tOFF-GC in response to threshold dendritic positive current steps (lower colored traces). Same cells as (C).

(E) Cell-class-specific pattern of AP backpropagation. Dendritic recording distance is expressed as a fraction of maximal dendritic path length. The lines represent single exponential fits to the data.

(F) Distance-dependent delay between somatically recorded APs and dendritically recorded BPAPs.

(G) Cell-class-specific time delay between regenerative activity (spikes) evoked by threshold dendritic current steps in sOFF and tOFF-GCs. Positive times describe the generation of dendritic spikes that preceded APs, whereas negative times reflect BPAPs.

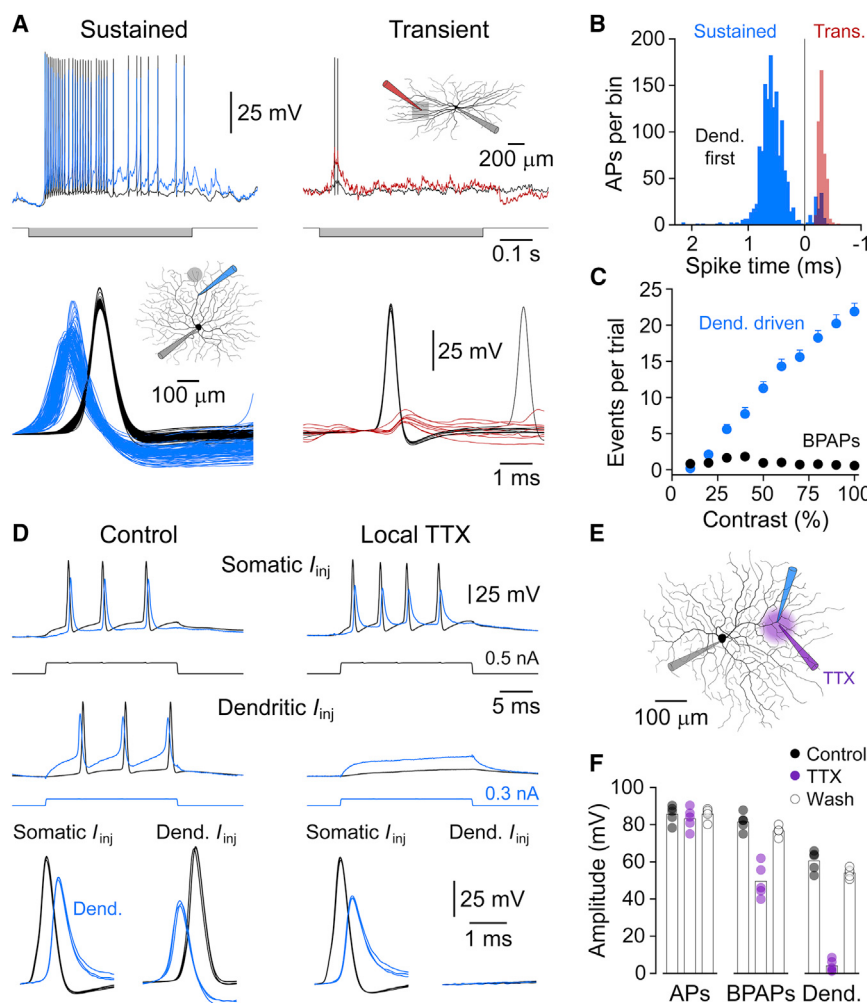
that cell-class-dependent signatures of dendritic excitability define the computational function of OFF-GCs.

RESULTS

Somatic whole-cell recordings were made from visually identified OFF-GCs maintained in whole-mounts of the ventral peripheral rabbit retina. Action potential (AP) firing of OFF-GCs was powerfully driven by the presentation of dark visual stimuli on a uniformly illuminated background that had a brightness equivalent to light intensity at dawn or dusk (luminance = 3.6×10^{11} quanta/cm²/s; Figures 1A and 1B). Analysis revealed two populations of OFF-GCs; sustained and transient, consistent with previous observations (Sanes and Masland, 2015). Sustained OFF (sOFF)-GCs fired APs throughout the presentation of flashed dark spot stimuli, whereas transient OFF (tOFF)-GCs predominantly fired APs as a high-frequency burst following stimulus onset (instantaneous frequency = 385 ± 4 Hz; Figures 1A and 1B). Morphologically, these classes of OFF-GC were quantitatively distinct, with sOFF-GCs having significantly

smaller, but more elaborate, dendritic trees (maximal dendritic diameter: sOFF = 637 ± 10 μ m, $n = 58$; tOFF = $1,392 \pm 24$ μ m, $n = 70$, Mann-Whitney, $p < 0.0001$; dendritic branch points: sOFF = 130 ± 4.1 $n = 36$; tOFF = 48.5 ± 1.1 , $n = 41$, Mann-Whitney, $p < 0.0001$; Figures S1A-S1E). The dendrites of both classes of OFF-GCs, however, radiated close to and parallel with the OFF-band of choline acetyltransferase immunostaining that defines the border of sublamina 2 of the inner plexiform layer (Figures S1F-S1H).

To examine the properties of dendritic excitability of these classes of GCs, we made whole-cell recordings from the dendrites and soma (Figures 1C-1F). Simultaneous somato-dendritic recordings revealed that APs, evoked by injection of threshold steps of somatic current, efficiently backpropagated into the dendritic tree of sOFF-GCs, exhibiting little distance-dependent amplitude decrement (current = 0.22 ± 0.02 nA; conduction velocity = 0.43 m/s; $n = 29$; Figures 1C, 1E, and 1F). In contrast, AP backpropagation in tOFF-GCs was decremental and demonstrated powerful distance-dependent attenuation (current = 0.40 ± 0.03 nA; conduction velocity = 0.88 m/s; $n = 52$; Figures 1C, 1E, and 1F). This diversity of electrical operations was more apparent when positive current steps were injected at dendritic sites (Figure 1D). In sOFF-GCs, fast and powerful dendritic spikes were initiated as a threshold response, which invariably forward propagated to the soma and axon to drive APs, when dendritic recordings were made at sites



>0.3 of the total dendritic path length, corresponding to a distance of 120 µm from the soma (dendritic spikes: amplitude = 62.0 ± 0.7 mV; rise-time = 0.27 ± 0.01 ms; half-width = 0.4 ± 0.01 ms; APs: amplitude = 91.5 ± 0.6 mV; rise-time = 0.27 ± 0.005 ms; half-width = 0.4 ± 0.004 ms; n = 102 events; Figures 1D and 1G). In contrast, the injection of threshold dendritic current steps in tOFF-GCs did not generate dendritic spikes, rather dendritic depolarization directly spread to the soma and axon to initiate AP firing, resulting in the generation of APs that were followed by small amplitude dendritic BPAPs (back-propagating action potentials) (Figures 1D and 1G). Such behavior may arise because of differences in the electrical structure of OFF-GC classes. For example, if the electrical structure of tOFF-GCs is compact, dendritic excitatory input is likely to efficiently spread to the axonal site of AP initiation, whereas if the electrical structure of sOFF-GCs is distributed, dendritic spike initiation may function to enhance the efficacy of dendritic excitatory input to mitigate for the effects of dendritic cable filtering (Williams and Stuart, 2002). Surprisingly, however, when we analyzed the distance-dependent attenuation of subthreshold voltage responses, the electrical structure of sOFF-GCs was found to be more compact than tOFF-GCs (Figures S2A–S2C).

Pooled analysis revealed that the dendro-somatic and somato-dendritic length constants of sOFF-GCs were 151 and 786 µm, respectively, and 168 and 558 µm in tOFF-GCs (Figures S2A and S2B). As the size of the dendritic tree of OFF-GCs are distinct, we also expressed these values as a fraction of dendritic path length, finding at a dendritic path length of 0.5 that dendritic voltage responses were attenuated to 0.30 at the soma and somatic responses to 0.73 at the dendrites of sOFF-GCs; whereas in tOFF-GCs, these values were 0.14 and 0.56, respectively (Figure S2C). Thus, dendritic spike generation does not simply function to overcome the distance-dependent properties of dendritic cable attenuation in OFF-GCs, as dendritic spike initiation was absent in the morphologically and electrically distributed population of tOFF-GCs; a finding which suggests that dendritic spike generation in sOFF-GCs may have a specialized role in the encoding of visual stimuli.

To test this idea, we first examined if dendritic spikes could be evoked in sOFF-GCs in response to visual stimuli projected at dendritic sites (Figure 2A). Simultaneous somato-dendritic recordings revealed that flashed dark spots reliably evoked dendritic spike initiation that preceded and drove AP firing (1,316 of 1,419 APs; spot size = 50–75 µm; contrast = 100%;

Figures 2A and 2B). Furthermore, input-output relationship revealed that dendritic spikes were initiated by low contrast stimuli (**Figure 2C**). In tOFF-GCs, however, dendritic dark stimuli did not evoke dendritic spikes but directly evoked sparse AP firing, despite the generation of robust dendritic synaptic depolarization (**Figures 2A and 2B**). To examine if this disparity arose as a product of our recording techniques, we examined the timing of regenerative activity in simultaneous somatic whole-cell and dendritic cell-attached recordings. In sOFF-GCs, dendritic cell-attached recording revealed that flashed dark spots evoked dendritic regenerative activity that preceded somatically recorded APs, whereas APs evoked by somatic current injection preceded extracellularly recorded BPAPs (spot size = 75 μm ; contrast = 100%; dendritic recording = $177 \pm 34 \mu\text{m}$ from the soma; n = 5; **Figures S2D and S2E**). In contrast, the timing of extracellularly recorded dark spot- and somatic current-evoked regenerative events were similar in tOFF-GCs, and, in all cases were first detected at the soma (spot size = 200 μm ; contrast = 100%; dendritic recording = $326 \pm 29 \mu\text{m}$ from the soma; n = 5; **Figures S2D and S2E**). Together, these data reveal that dendritic excitatory input is locally integrated in sOFF-GCs and drives dendritic spike initiation. In contrast, in tOFF-GCs, dendritic excitatory input driven by dark visual stimuli directly drives AP firing. Moreover, in tOFF-GCs, a similar sequence of regenerative activity was generated at the offset of flashed light stimuli, despite the generation of large amplitude transient dendritic depolarization, which increased in amplitude to >30 mV as light spots were presented at increasingly remote dendritic recording sites (**Figures S3A–S3E**). As this distance-dependent increase in light response amplitude could be replicated by the injection of uniform dendritic current waveforms (**Figures S3F–S3I**), these data suggest that the amplitude of dendritic light responses are shaped by the electrical architecture of tOFF-GCs. Taken together, therefore, our findings reveal distinct modes of dendritic integration in classes of OFF-GCs, with tOFF-GCs exhibiting passive dendritic integration and sOFF-GCs active dendritic integration. To explore the ionic mechanisms underlying active dendritic integration in sOFF-GCs, we locally applied the sodium channel blocker tetrodotoxin (TTX; 3 μM) to dendritic sites of sOFF-GCs, reasoning that the fast current- and light-evoked dendritic spikes are mediated by the regenerative activation of sodium channels ([Oesch et al., 2005](#); [Sivyer and Williams, 2013](#)). Indeed, the local pressure application of TTX to sites close to the dendritic recording electrode eliminated the generation of dendritic spikes and significantly decreased the amplitude of BPAPs, in a reversible manner (**Figures 2D–2F**). In contrast, the local dendritic application of TTX did not alter the somatic amplitude of APs triggered by somatic current steps, directly demonstrating that dendritic spikes are mediated by the activation of dendritic sodium channels in sOFF-GCs (**Figures 2D–2F**).

To examine how this cell-class-specific expression of active dendritic integration contributes to computation, we presented a suite of dark visual stimuli moved across the retinal surface (**Figure 3**). Moving dark bars reliably evoked trains of APs in sOFF-GCs over a wide speed range (0.5–7 mm/s; dark bar: height = 500 μm , width = 200 μm ; contrast = 100%; **Figures 3A and 3B**). In contrast, tOFF-GCs did not respond to dark bars moved at relatively slow speeds but sparsely fired APs in

response to faster moving stimuli (**Figures 3A and 3B**). In sOFF, but not tOFF-GCs, AP firing was first generated at times when the moving stimulus approached the edge of the dendritic tree of the recorded cell (**Figure 3A**), ensuring that the size of the suprathreshold receptive field, calculated from the time of generation of the first and last light-evoked AP, was preserved, across the entire speed range investigated (**Figure 3C**). Indeed, across trials, we found a close to unity relationship between the size of the dendritic tree and the suprathreshold receptive field (**Figure 3D**). Although the rate of AP firing was related to the speed of movement in both classes of OFF-GCs, such relationship were quantitatively different, with the AP firing rate of sOFF-GCs increasing exponentially to reach a plateau as the stimulus speed was increased (**Figure 3E**), a relationship mirrored by a roughly parallel shift in the distribution of instantaneous AP firing frequency (**Figure S4A**). The relatively low firing rate of tOFF-GCs was, however, dominated by the generation of high-frequency AP bursts and so was unrelated to the speed of movement (**Figures 3A and S4A**). The remarkable precision with which sOFF-GCs responded to moving stimuli was preserved when the size and contrast of dark bars were altered (**Figures 3F and 3G; Figure S4B**). Notably, this sensitivity of sOFF-GCs was apparent across a wide range of background luminance, spanning the scotopic to photopic range (luminance = 1.3×10^9 – 1.2×10^{13} quanta/cm²/s; **Figure S5**). In contrast, tOFF-GCs responded weakly to large dark bars moved at slow speeds but progressively generated AP firing in response to large dark stimuli moved at faster speeds, consistent with the role in signaling looming visual images ([Münch et al., 2009](#); [Wang et al., 2021](#); **Figures S4C and S4D**). Indeed, we observed that tOFF-GCs reliably responded to expanding dark visual stimuli, maintaining AP firing as stimuli were expanded within, and beyond the dendritic field (**Figures S4F–S4H**). In contrast, sOFF-GCs, first generated AP firing in response to expanding visual stimuli at times before transient-OFF GCs, consistent with the detection of small sized stimuli, but failed to maintain AP firing as the visual stimuli expanded beyond their dendritic fields (**Figures S4F–S4H**).

To reference the visual stimuli that activate sOFF-GCs to real-world objects we calculated, using a measured nodal distance of 9.8 mm ([Hughes, 1972](#)), that a bird of prey with wingspan of 1 m, and wing thickness of 0.1 m, flying 25 m from the eye of a rabbit would cast a dark retinal image of 390 by 39 μm . At this distance, a speed of movement of 50 km/h corresponds to a retinal displacement of 5.45 mm/s. Thus, sOFF-GCs respond with high precision to ethologically appropriate moving visual stimuli across a wide range of background luminance.

We next explored if the AP output of sOFF-GCs was directionally tuned by presenting dark bars moved in one of twelve directions across the receptive field (**Figure 4A**). The AP firing of sOFF-GCs was similar in all directions, yielding circular Rayleigh plots of AP output (**Figure 4C**). Notably, this circularity of AP output was mirrored by a circularity of dendritic morphology, when the diameter of the dendritic tree was measured along the axis traversed by the dark stimuli (**Figure 4D**), underpinning our observation of a close correspondence between the size of the dendritic tree and the suprathreshold receptive field. These findings suggest a mechanistic framework in which to understand previous

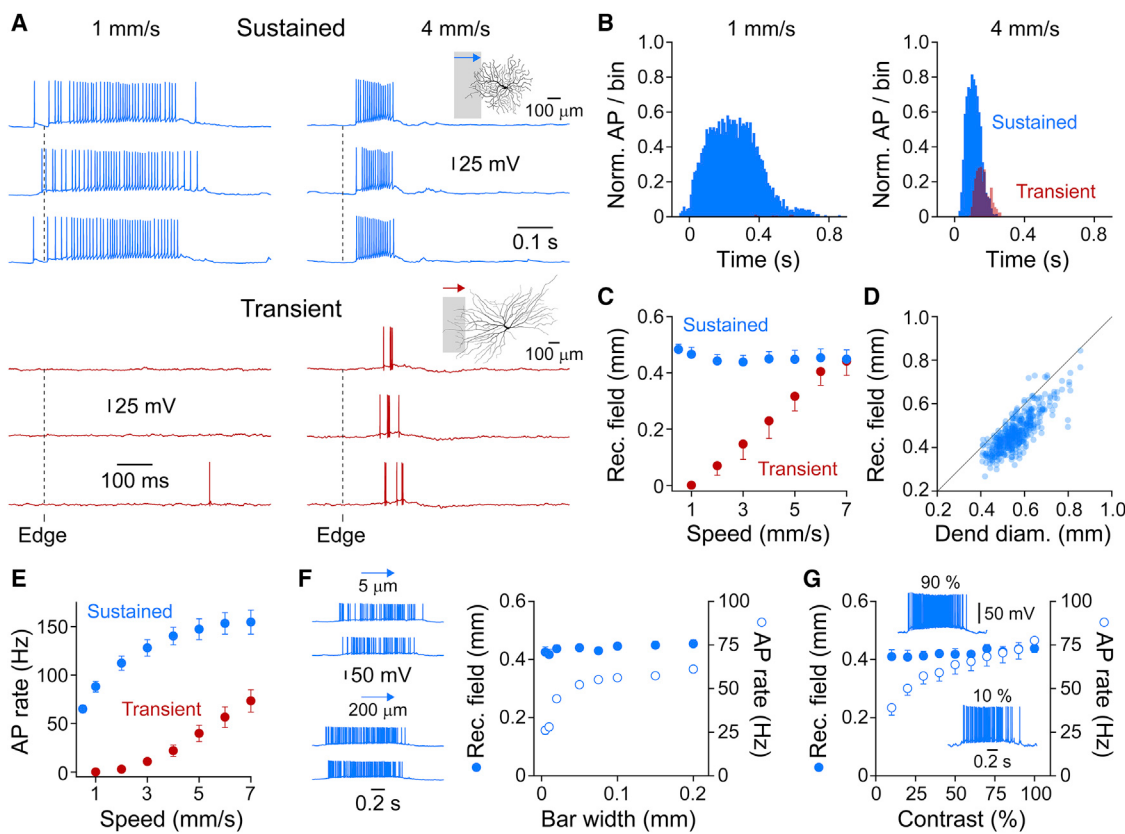


Figure 3. Cell-class-specific encoding of motion by OFF-GCs

- (A) Moving dark bars of the indicated speed evoke robust AP firing in sOFF, but not tOFF-GCs. Morphology and visual stimuli are shown inset. The time point where the leading edge of the stimulus entered the dendritic territory is indicated (Edge).
- (B) Normalized peristimulus time histograms (PSTHs) of moving dark bar-evoked AP firing of sOFF (blue, n = 13) and tOFF (red, n = 9) GCs. PSTHs were computed in each cell, peak scaled to 1 and then averaged.
- (C) Relationship between suprathreshold receptive field size and dark bar speed in sOFF (n = 13) and tOFF (n = 9) GCs.
- (D) Relationship between suprathreshold receptive field size and the dendritic field diameter of sOFF-GCs, measured along the axis of dark bar movement (speed = 0.5 mm/s, n = 444 trials, n = 37). The line has a unity slope.
- (E) sOFF (n = 13) and tOFF (n = 9) GCs differentially encode the speed of dark bar movement in AP firing rate.
- (F) The receptive field size of sOFF-GCs (n = 4) is not determined by the width of moving dark bars (speed = 0.5 mm/s). Note that AP firing rate encoded bar width. The inset shows representative responses evoked by dark bars of the indicated width.
- (G) Receptive field size of sOFF-GCs is not determined by the contrast of moving dark bars (speed = 0.5 mm/s, n = 6). Note that stimulus contrast is encoded in the rate of AP firing. The inset shows that representative responses evoked by dark bars of the indicated contrast.

Values in (C) and (E)–(G) represent mean ± SEM.

observation of anticipatory AP firing in OFF-GCs of the rabbit and salamander retinas (Berry et al., 1999). Consistent with previous reports, flashed dark bars aligned to the center of the soma of sOFF-GCs evoked AP firing following a short transduction delay (delay = 42.3 ± 0.4 ms, number of trials = 241; Figure 4B). In contrast, when time zero was set to the time when moving dark bars excited the center of the soma, analysis revealed that AP firing proceeded that evoked by soma-centered flashed dark bars, a behavior that emerged as a product of AP firing first occurring at times when the leading edge of the moving stimuli approached the edge of the dendritic tree of sOFF-GCs (Figures 4A and 4B). Such characteristics suggests that sOFF-GCs may signal the local movement of objects in the visual world, as opposed to the global movement of the visual

world imparted by movement of the head or eyes (Olveczky et al., 2003). To test this, we presented moving grating stimuli (0.5 mm/s, dark bar width = 250 μm) that were either spatially restricted to the average size of the dendritic tree of sOFF-GCs or presented more globally across retinal space (Figures 4E–4G). Strikingly, we found that local, receptive field delineated, stimuli evoked AP firing that was significantly greater than those evoked by larger global stimuli, suggesting that activation of the receptive field surround acts to inhibit AP firing generated as the stimulus excited the receptive field (Figures 4E–4G). Taken together, our findings, therefore, reveal that sOFF-GCs encode the local motion of visual stimuli, by first generating AP firing at time points when dark bars approach the edge of the dendritic tree; a behavior that suggests local motion is encoded by active dendritic integration

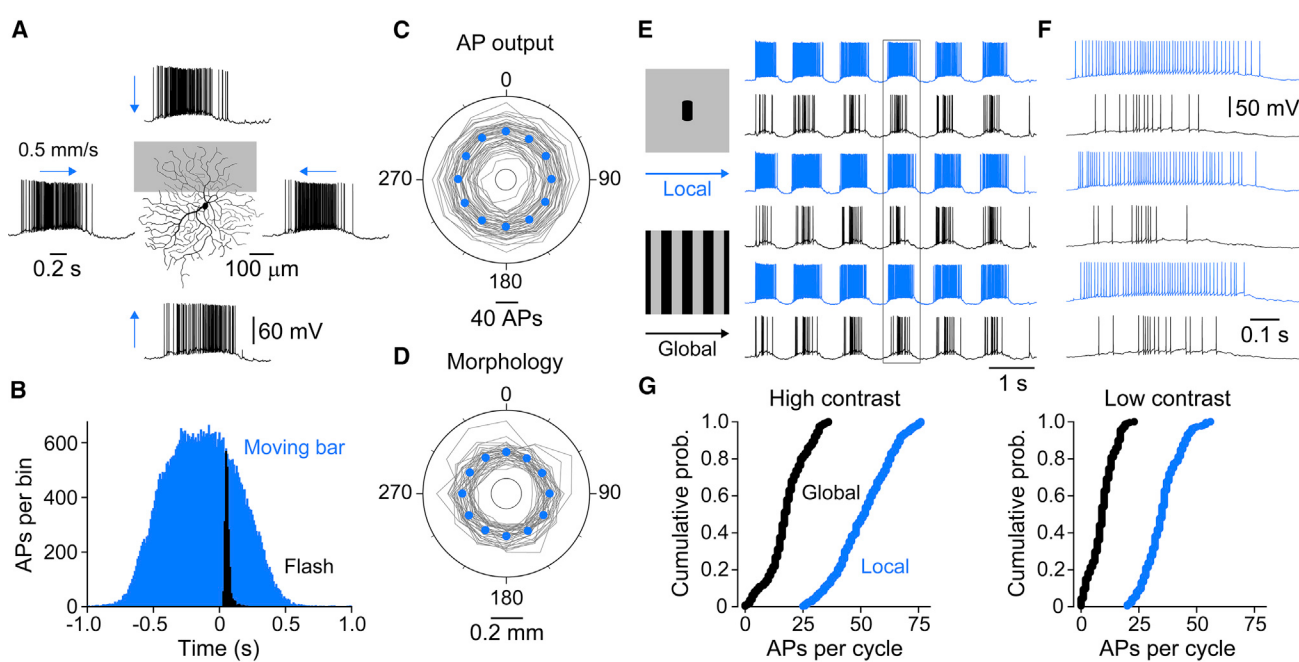


Figure 4. Sustained OFF-GCs encode local motion

(A) AP firing of a sOFF-GC evoked by dark bars moved in the indicated directions. The morphology of the cell is shown.
(B) Peristimulus time histogram of AP firing evoked by a soma-centered flashed (15 ms) dark bar (black), or when the same bar was moved at a speed of 0.5 mm/s across the receptive field (blue). Time zero corresponds to the time point when the moving dark bar was centered on the soma.
(C) Rayleigh plot of average AP firing evoked in sOFF-GCs by dark bars moved in 12 directions ($n = 46$ cells, blue symbols). The gray lines represent each cell.
(D) Rayleigh plot of dendritic diameter measured along the axis traversed by moving dark bars. Same convention as (C).
(E and F) AP responses of a sOFF-GC evoked by the local (blue) or global motion of gratings (bar width = 250 μm, speed = 0.5 mm/s). The boxed cycles are shown at a faster time base (F). Local stimuli were restricted to a circular area (size = 500 μm, centered at the soma).
(G) Cumulative probability distributions of AP firing evoked during each cycle of local (blue) or global motion (black) of high (100%; $n = 9$) or low (20%, $n = 7$) contrast stimuli. Distributions are significantly different, t test; 100%, $p < 0.0001$; 20%, $p < 0.0001$.

(Oesch et al., 2005; Sivyer and Williams, 2013; Velté and Masland, 1999), operational at sites throughout the dendritic tree of sOFF-GCs.

To test this idea, we recorded AP firing driven by moving dark bars at the resting membrane potential of sOFF-GCs, and then injected negative current through the somatic recording electrode to hyperpolarize the somatic membrane away from AP initiation threshold, reasoning that this would reveal the somatic consequence dendritic spike generation in isolation (Oesch et al., 2005; Figure 5). When the somatic membrane was hyperpolarized, moving dark bars evoked barrages of small amplitude, fast rising, and decaying spike-like potentials, which we term spikelets (negative current = 1.1 ± 0.1 nA; membrane potential = -86.7 ± 2.4 mV; spikelet: amplitude = 9.20 ± 0.16 mV, rise-time = 0.44 ± 0.01 ms, half-width = 0.97 ± 0.01 ms; APs (from rest): amplitude = 75.9 ± 0.1 mV, rise-time = 0.36 ± 0.002 ms, half-width = 0.47 ± 0.001 ms; Figure 5A). Remarkably, the receptive fields delineated by the generation of spikelets, recorded during somatic hyperpolarization, were similar in size to those defined by AP firing at resting membrane potential (Figures 5B and 5C), suggesting that AP firing is reliably driven by dendritic spikes, a notion consistent with the relatively rare observation of isolated spikelets at resting membrane potential (Figure 5B).

We next directly examined if dendritic spikes were evoked by moving dark stimuli (Figure 6). As a first step, we digitally aver-

aged dendritic voltage responses across multiple trials to define the time point at which moving dark bars first drove dendritic synaptic depolarization of OFF-GCs (Figure S6A), a critical factor in relating the location of moving stimuli of different speeds with dendritic geometry (Figures 6A–6C). Analysis revealed that sOFF-GCs first generated APs in response to dark bars at a latency of 16.9 ± 0.83 ms after the onset of dendritic synaptic depolarization. In contrast, moving stimuli evoked sparse AP firing with a longer latency (73.1 ± 1.12 ms) in tOFF-GCs (Figures 6A and 6C). When we converted such latencies into the distance traversed by moving dark bars, analysis revealed that dark bars first evoked AP firing in sOFF-GCs as the leading edge of dark bars crossed the edge of the dendritic tree (Figure 6C). At these sites, simultaneous somatic-dendritic recording of sOFF-GCs revealed that dendritic spikes preceded and drove AP firing, as dark bars entered the receptive field and moved toward the dendritic recording site, until at time points when the leading edge of moving dark bars passed the dendritic recording site and approached the soma and moved into the contralateral dendritic tree, where regenerative events were first detected at the soma and APs backpropagated to the dendritic recording site (Figures 6D and 6E). In contrast, in tOFF-GCs, regenerative events evoked by moving dark bars were always detected first at the soma and APs backpropagated into the dendritic tree (Figures 6D and 6E). Notably, in sOFF-GCs, the fraction of APs

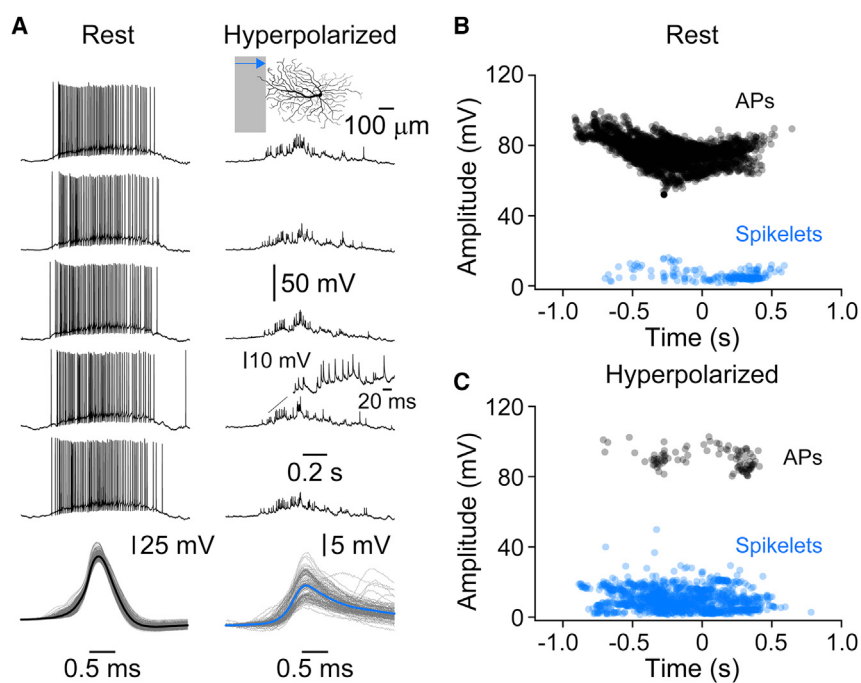


Figure 5. Somatic membrane hyperpolarization reveals spike-like potentials in sustained OFF-GCs

(A) Regenerative activity evoked by a moving dark bar (0.5 mm/s) recorded from the soma of a sOFF-GC at resting membrane potential (rest) and during somatic hyperpolarization (-85 mV). The lower overlain traces show detected APs recorded from rest (black line is a digital average) and spike-like potentials (spikelets) at the hyperpolarized potential (blue line is a digital average). Morphology and dark stimuli are shown inset.

(B and C) Amplitude of regenerative events at resting (B) and hyperpolarized membrane potentials (C, -86.7 ± 2.4 mV, $n = 9$). Time zero corresponds to a time point when the moving stimuli were soma centered.

driven by dendritic spikes was similar when the speed of dark bar movement was varied across a wide range (Figures 6F and S6B–S6D). It should be noted that this fraction reflects only the regenerative events generated in areas of the dendritic tree that fed the dendritic recording site and so constitutes only a portion of the total number of dendritic spikes generated across the entire dendritic tree, which is reflected, more faithfully, by the analysis of spikelets following somatic hyperpolarization (Figure 5). Consistent with this interpretation, dendritic spikes that preceded AP firing were generated when dark bars were swept in opposite directions across the receptive field, at sites when the leading edge of the dark bar moved close to the dendritic recording site (Figure 6G).

How is this active dendritic integration mechanism controlled by stimuli that coherently activate areas of visual space surrounding the receptive field of sOFF-GCs, a pattern that occurs during global motion? To examine this, receptive field delineated dark spot stimuli centered at the soma of recorded sOFF-GCs were presented, and in interleaved trials, a dark surround of variable inner diameter was simultaneously projected (dark soma-centered spot diameter = 250 μm; surround: outer diameter = 4,000 μm, inner diameter = 500–3,500 μm, contrast = 100%; Figure 7A). Analysis revealed that the simultaneous presentation of a dark surround efficiently inhibited the AP firing evoked by the central dark spot, an effect that was maximal when the inner diameter of the surround was small and decreased as the surround was made more peripheral (Figure 7B). We next explored how such surround inhibition-controlled AP firing evoked by moving stimuli, by presenting a dark surround at a time when the leading edge of the dark bar was 100 μm from the somata of recorded sOFF-GCs (dark surround inner diameter = 1 mm, contrast = 100%, moving bar size: height = 500 μm, width = 200 μm, contrast = 20%, speed = 0.5 mm/s). In each sOFF-

GC tested, the dark surround either abolished or significantly decreased the AP firing evoked by moving dark bars (Figures 7C and 7D). To examine the factors that influence this, the surround stimulus was presented in isolation, revealing inhibition characterized by membrane hyperpolarization that first peaked and then slowly decayed with a roughly exponential time course, a time course that mirrored the inhibition of AP firing (Figures 7C and 7E). Notably, simultaneous recordings revealed that the peak amplitude of membrane hyperpolarization evoked by surround stimuli was uniform at somatic and dendritic recording sites (somatic hyperpolarization = -7.7 ± 1.16 mV; dendritic hyperpolarization = -7.8 ± 1.04 mV; average dendritic recording location = 147 ± 9.6 μm from the soma [$n = 5$]). As AP firing is driven by the generation of dendritic spikes in sOFF-GCs, these data suggest that surround inhibition should control active dendritic integration. To test this, we injected short steps (10 ms) of dendritic current to drive dendritic spike initiation under control conditions and following the presentation of a surround dark stimulus (surround stimulus inner diameter = 1 mm; contrast = 100%; Figure 7F). Surround inhibition was found to abolish the initiation of dendritic spikes in response to dendritic current steps delivered at the current threshold determined under control (Figure 7F). Pooled analysis revealed that surround inhibition increased the magnitude of the dendritic current required to initiate dendritic spikes in sOFF-GCs, in a manner consistent with subtractive inhibition (control dendritic current rheobase = 0.22 ± 0.02 nA; surround dendritic current rheobase = 0.44 ± 0.07 nA, $p = 0.011$, t test; $n = 5$; Figure 7G, upper graph). In the presence of surround inhibition dendritic spikes generated by larger amplitude dendritic current steps faithfully forward propagated to drive AP firing, resulting in a near identical rightward shift in the value of dendritic current required to drive AP output (failed dendritic spikes: control = 1 of 193; surround = 1 of 131; Figure 7G, lower graph). Thus, surround inhibition powerfully controls the initiation of dendritic spikes evoked by moving visual stimuli, revealing a mechanism by which global stimuli control the AP output of sOFF-GCs.

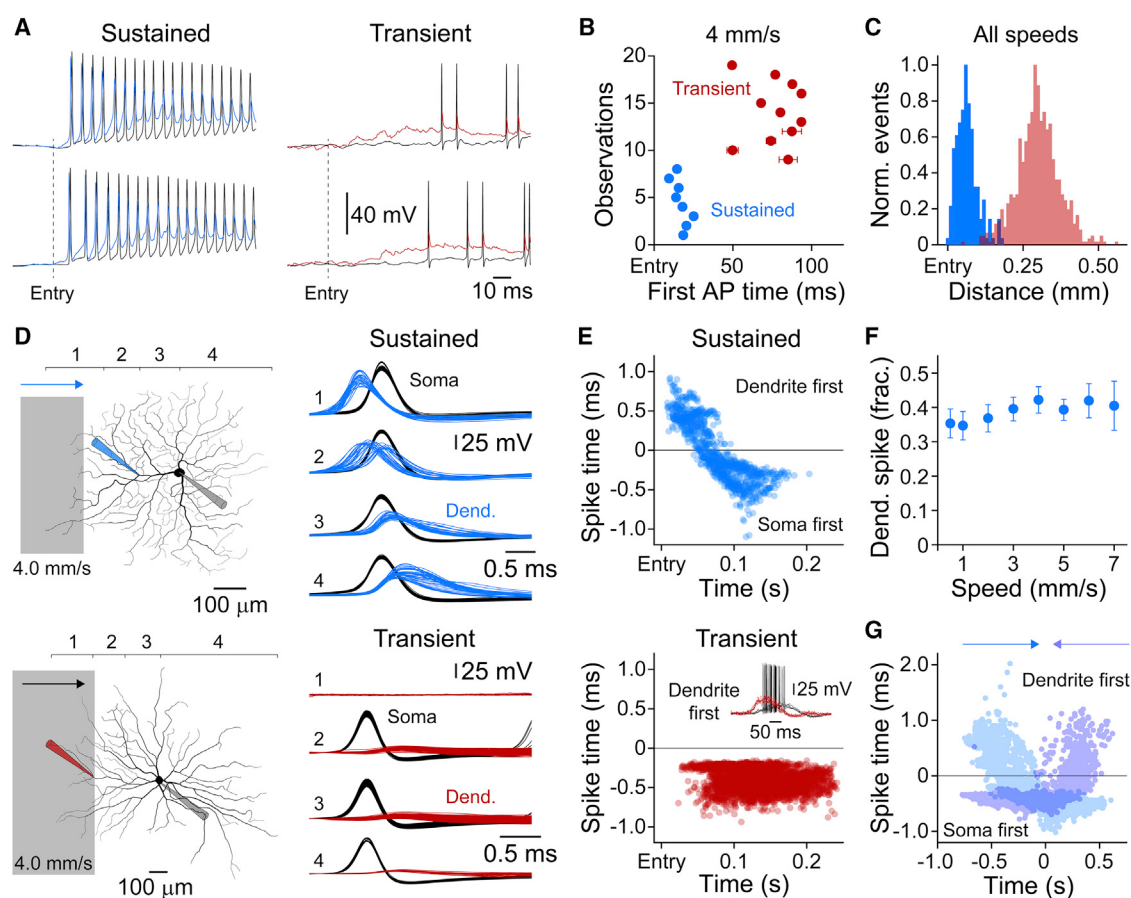


Figure 6. Dendritic spikes are driven by image motion in sustained OFF-GCs

(A) Somatic-dendritic recording of voltage responses evoked by moving dark bars (speed = 4 mm/s) demonstrate that AP firing is evoked at short latency following the onset of dendritic synaptic depolarization (Entry) in sOFF, but not tOFF-GCs.

(B) Average latency to AP firing for sOFF and tOFF-GCs following the generation of dendritic synaptic depolarization (Entry) in response to dark bars moved at the indicated speed. Values represent mean \pm SEM.

(C) sOFF but not tOFF-GCs fire APs near the leading edge of moving dark bars. The spatial position of first AP generation is expressed relative to the onset of dendritic depolarization (Entry). Responses to dark bars moved at speeds of 0.5–7 mm/s have been pooled (sOFF, n = 187 trials, n = 9; tOFF, n = 788 trials, n = 11).

(D) Moving dark bars evoke dendritic spikes which precede and drive APs in sOFF, but not tOFF-GCs. The traces show overlaid somatic (black) and dendritic regenerative events (colored), generated when moving dark bars were located at the position highlighted on the reconstruction of the recorded sOFF and tOFF-GC, which also indicates the placement of recording pipettes.

(E) Pooled data show that spikes are first generated at dendritic sites in sOFF-GCs when moving dark stimuli enter and sweep across the dendritic tree (average dendritic recording location = $133 \pm 11 \mu\text{m}$ from the soma). In contrast, in tOFF-GCs, APs always proceeded backpropagating APs (average dendritic recording location = $346 \pm 37.4 \mu\text{m}$ from the soma). The inset shows the dendritic synaptic depolarization (red) evoked by a moving dark bar in the tOFF-GC shown in (D).

(F) Fraction of APs driven by dendritic spikes is not related to dark bar speed in sOFF-GCs (n = 4, mean \pm SEM).

(G) Timing of regenerative events generated in sOFF-GCs when dark bars were swept in opposite directions across the receptive field. Note the generation of dendritic spikes when dark stimuli were moved in either direction (n = 30 trials, n = 6, speed = 0.5 mm/s).

The tracking of moving objects across space requires the encoding of image motion by adjacent GCs, as visual images sweep across the retina. Anatomical classes of GCs are known to be tiled, where the terminal dendritic tips of OFF-GCs interdigitate (Peichl, 1991; Wässle et al., 1981). To experimentally test if such tiling allows an unbroken representation of image motion across visual space, we made simultaneous somatic recordings from nearest neighbor pairs of OFF-GCs and swept dark bars progressively across the receptive fields of recorded cells (Figure 8A). When nearest neighbor pairs of sOFF-GCs were recorded, moving dark bars evoked AP firing as the dark bar ap-

proached and moved across the dendritic tree of the first cell, and then into the receptive field of the second cell, resulting in a period during which AP firing overlapped in time in both sOFF-GCs (Figures 8A, S7A–S7C, and S8A–S8C). This period of co-firing was apparent in all recorded nearest neighbor sOFF-GC pairs and was manifest in response to small sized moving visual objects (75 by 75 μm ; Figures S8A–S8C). In contrast, AP co-firing was largely absent in nearest neighbor pairs of tOFF-GCs, which generated fragmented patterns of AP firing in response to large sized moving bars, and failed to respond to smaller moving objects (Figures 8A, 8B, S7A–S7C,

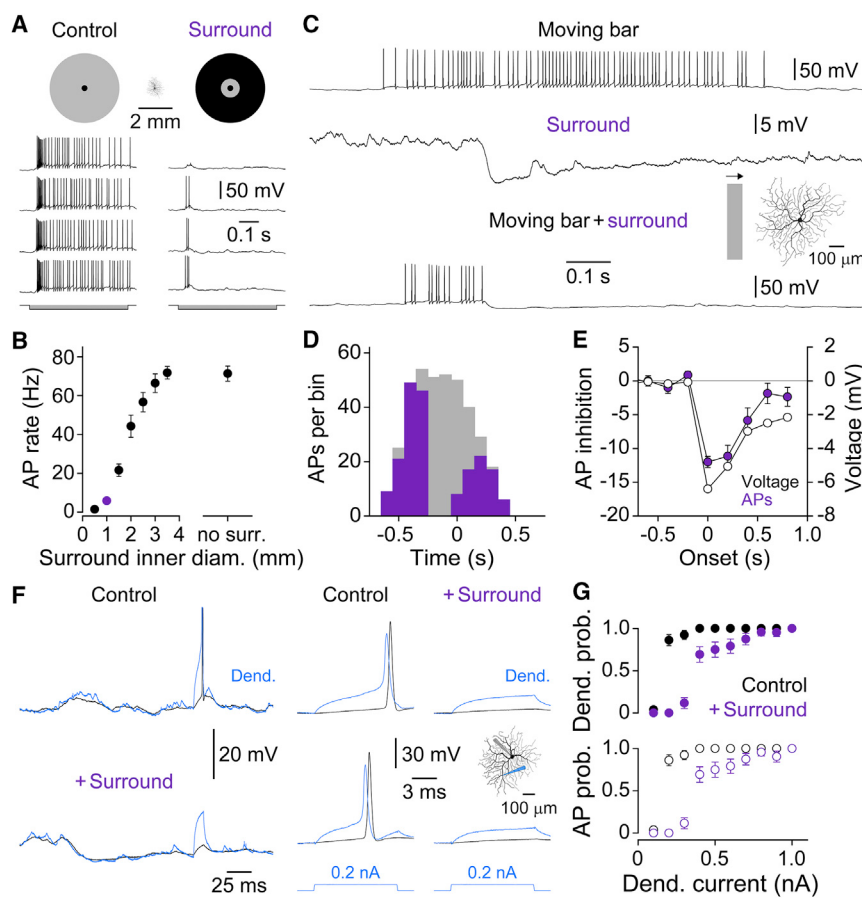


Figure 7. Surround inhibition controls dendritic spike generation in sustained OFF-GCs

(A) Dark surround stimuli suppress AP firing evoked by receptive field centered dark spots (diameter = 250 μ m). The lower trace shows the stimulus time course. Morphology and visual stimuli are shown inset.

(B) Relationship between AP firing rate and the inner diameter of surround stimuli. Note the declining influence as the inner diameter of the surround was increased. The colored symbol refers to the surround shown in (A).

(C) Surround stimuli suppress AP firing evoked by moving dark bars. Voltage traces show responses evoked by the movement of a dark bar (contrast = 20%, speed = 0.5 mm/s), the presentation of a dark surround (inner diameter = 1 mm, contrast = 100%), and the conjoint presentation of stimuli. Morphology is shown inset.

(D) Peristimulus time histogram of AP firing evoked by moving dark bars presented alone (gray) or conjointly with surround stimuli (purple). Note the reduction of AP firing evoked by surround stimuli projected 0.2 s before the moving dark bar approached the soma (time = 0, n = 7). (E) Time course of membrane hyperpolarization (open symbols, dark surround alone, 100 ms time bins, n = 7, mean \pm SEM), and reduction of the number of dark moving bar-evoked APs (colored symbols) by surround stimuli. Time = 0 refers to the onset of the surround. The reduction of AP firing is expressed relative to the presentation of the moving bar alone.

(F) Somato-dendritic recording of membrane hyperpolarization evoked by surround stimuli and responses are shown at a faster time base (right).

(G) Surround stimuli increases the dendritic current required to initiate dendritic spike generation (upper graph) and consequential AP firing (lower graph). Probability was calculated across trials (n = 5 cells, mean \pm SEM).

the annihilation of dendritic current step-evoked dendritic spike generation. Current step-evoked responses are shown at a faster time base (right). Morphology and electrode placement is inset.

(G) Surround stimuli increases the dendritic current required to initiate dendritic spike generation (upper graph) and consequential AP firing (lower graph). Probability was calculated across trials (n = 5 cells, mean \pm SEM).

and S8A–S8C). This disparity emerged despite the similar degree of anatomical overlap between the dendritic trees of nearest neighbor pairs of sOFF and tOFF-GCs (Figures 8C and S7A–S7C). The uninterrupted pattern of AP firing in sOFF-GCs was preserved when the speed of the moving bars, or the stimulus area, was varied across a wide range, resulting in a steady fraction of stimulus-evoked APs generated in the co-firing period (Figures 8D, 8E, and S8A–S8C). Analysis revealed that AP co-firing was not dependent on junctional connectivity between sOFF-GCs, as we found no evidence for gap-junctional or synaptic interactions (Figures 7D–7G). Thus, the dendritic-spanning suprathreshold receptive field properties of sOFF-GCs, formed by the generation of dendritic spikes, leads to an uninterrupted wave of AP firing that travels across retinal space as objects move through the visual world.

DISCUSSION

The retina allows direct interrogation of the cellular and circuit mechanisms that signal and compute natural stimuli. Surprisingly, therefore, the role of active dendritic integration in such

computations has previously been directly addressed in only one of the ~30 functionally and anatomically defined classes of retinal GCs that send abstractions of the visual world to the higher brain (Baden et al., 2016; Sanes and Masland, 2015). Given the heterogeneity of the properties and expression of active dendritic integration across, and within, the multiple classes of neurons that form forebrain neuronal circuits (Cembrowski and Spruston, 2019; Fletcher and Williams, 2019; London and Häusser, 2005; Stuart and Spruston, 2015), we examined if the dendritic integrative properties of retinal GCs were cell-class specific. Strikingly, we find divergent patterns of dendritic integration in classes of OFF-GCs: sOFF-GCs that exhibited active dendritic integration and tOFF-GCs that exhibited passive dendritic integration. This functional divergence was accompanied by stereotyped differences in the size and branching structure of their dendritic trees. Notably, the passive dendritic trees of tOFF-GCs, which exhibited a characteristic α -morphology (Peichl, 1991; Wässle et al., 1981), were anatomically and electrically more distributed than sOFF-GCs. The dendrites of both classes of OFF-GCs, however, radiated at similar levels in the inner plexiform layer, consistent with previous description of

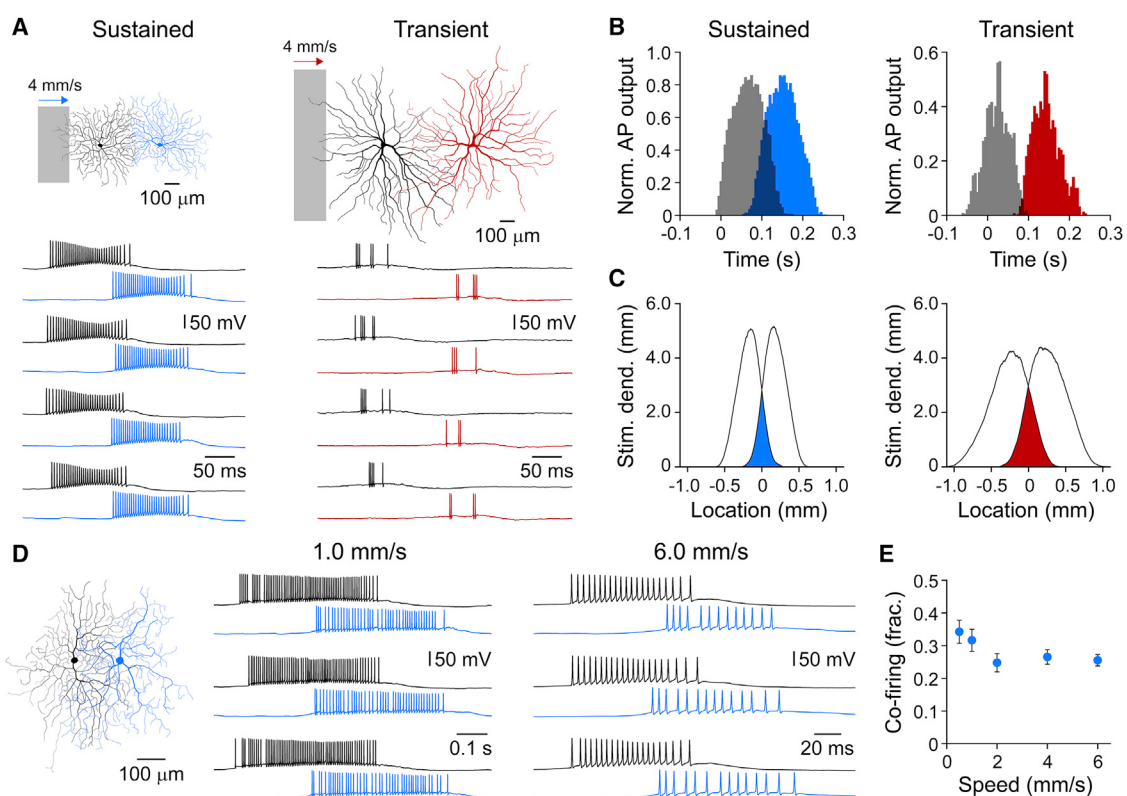


Figure 8. Encoding of image motion by tiled sustained OFF-GCs

(A) AP firing evoked by moving dark bars in nearest neighbor pairs of sOFF (black and blue traces) and tOFF (black and red traces) GCs as stimuli moved across retinal space. The morphology of GC pairs is shown inset. Note the overlap between the dendritic trees of nearest neighbor pairs, but the period of AP co-firing in sOFF, but not tOFF-GCs.

(B) Normalized peristimulus time histograms (PSTHs) of AP firing evoked in nearest neighbor pairs of sOFF ($n = 13$) and tOFF ($n = 8$) GCs. Note the overlap in PSTHs compiled from sOFF-GCs. Time = 0 refers to the time point when the moving dark bars were aligned to the soma of the first (black) cell.

(C) Histograms of dendritic segment length occupied by moving stimuli as they swept across dendritic trees, referred to as stimulated (stim.) dendritic length. The overlap between stimulated dendritic segments of nearest neighbor OFF-GCs is shaded. Location = 0 refers to the point of maximal overlap.

(D) A period of AP co-firing is apparent when dark bars are moved at different speeds. The morphologies of the recorded nearest neighbor sOFF-GCs are shown inset.

(E) Fraction of stimulus-evoked APs generated in the co-firing period is stable across a wide speed range ($n = 4$ nearest neighbor sOFF-GCs, mean \pm SEM).

genetically labeled PV4 and PV5 OFF-GCs of the mouse (Farrow et al., 2013) and tOFF-GC and sOFF-GCs of the guinea pig retina (Beaudoin et al., 2019). As the sustained or transient signaling of GC classes are thought to be inherited from presynaptic bipolar cells (Awatramani and Slaughter, 2000), their principal source of excitatory synaptic input (Sanes and Masland, 2015), the divergent integration strategies we report are likely to underlie specific neuronal and circuit computations. Consistent with this, we found that the active dendritic integration enabled the computation of the local motion of ethologically relevant visual stimuli by sOFF-GCs.

The heterogeneity of integration mechanisms we describe for classes of OFF-GC provides a framework in which to mechanistically understand the class-specific computations implemented within the wide and highly branched dendritic arbors of GCs in the peripheral retina. Direct dendritic recording from sOFF-GCs, and direction-selective ON-GCs (Brombas et al., 2017; Sivyer and Williams, 2013), has revealed that the local dendritic integration of light-evoked excitatory synaptic input results in

the generation of dendritic spikes which powerfully forward propagate to the soma and axon to drive AP firing. Across the space-filling dendritic trees of these classes of GCs, which sample a large fraction of the underlying array of bipolar cell-mediated excitatory input (Brown et al., 2000; Vaney et al., 2012; Figure S9), active dendritic integration functions to form suprathreshold receptive field properties defined by the geometry of the dendritic tree. Sensitivity to moving visual stimuli naturally arises in such a system, as local active dendritic integration occurs on a timescale defined by the relatively brief dendritic time constant (Williams and Stuart, 2003) and is reliably translated into AP output by the secure initiation and forward propagation of dendritic spikes, which can be driven at high frequencies (Sivyer and Williams, 2013). It should be noted that calcium imaging and somatic recordings from related classes of ON-OFF direction-selective GCs in the rabbit and murine retinae provide further evidence for the engagement of such active dendritic integration mechanisms (Jain et al., 2020; Oesch et al., 2005; Trenholm et al., 2014), suggesting a common

mechanistic framework for the computation of motion. Motion selectivity in these GC classes is achieved by the inhibitory synaptic control of active dendritic integration, which in sOFF-GCs is driven by the activation of areas of retinal space surrounding the receptive field (Buldyrev and Taylor, 2013), to evoke widespread somato-dendritic hyperpolarizing inhibition, which acts to increase the dendritic excitatory input required to reach the threshold for dendritic spike initiation. The attenuation of AP output of sOFF-GCs by global motion is therefore implemented by the subtractive inhibitory synaptic control of dendritic spike initiation. This process is mechanistically similar to the inhibitory synaptic control of direction-selective ON-GCs, which is achieved by the more refined local control of terminal dendritic spike initiation (Brombas et al., 2017; Sivyer and Williams, 2013). In both cases, however, inhibition does not function to veto the forward propagation of dendritic spikes but rather acts to control the initiation of dendritic spikes, consistent with simulation data which suggest that the magnitude of inhibitory synaptic conductance is insufficient to overcome the regenerative sodium conductance (Schachter et al., 2010).

In contrast, direct dendritic recordings of tOFF-GCs revealed that excitatory synaptic input is not actively integrated in the dendritic tree but is funneled from the dendritic site of generation to the soma and axon to be integrated solely at the axonal site of AP initiation. The absence of active dendritic integration mechanisms in tOFF-GCs does not, however, imply that local interactions between dendritic excitatory and inhibitory synaptic input (Koch et al., 1983) does not occur but reveals that the results of such synaptic interactions are integrated exclusively at the site of AP initiation. As a result of this integration scheme, tOFF-GCs are relatively insensitive to visual stimuli that excite small regions of the distal dendritic tree. Consistent with this, the structure of the dendritic trees of tOFF-GCs were found to be relatively sparse, ensuring the sampling of a low fraction of bipolar excitatory input (Brown et al., 2000; Schwartz et al., 2012; Figure S9). We note, however, that previous work has revealed that the receptive field properties of tOFF- α GCS are additionally influenced by gap-junctional connectivity, both with other tOFF- α GCS and classes of amacrine cells (DeVries, 1999; Völgyi et al., 2013). A further consequence of passive dendritic integration is diminished responsiveness to a wide range of motion stimuli, but sensitivity to larger faster moving visual objects. This property can be explained by passive cable attenuation, which acts to attenuate the amplitude of synaptic potentials as they spread from the dendritic site of generation to the soma and proximal axon (Rall, 1967; Williams and Stuart, 2002), ensuring that only visual input produced by excitation that is summed in space and time reaches the threshold for axonal AP initiation (Figure S4). Consistent with this, tOFF-GCs are known to be responsive to large, dendritic tree encompassing, visual input such as looming stimuli (Münch et al., 2009; Wang et al., 2021). Indeed, the selective ablation of tOFF- α GCS diminishes behavioral escape responses evoked by such stimuli in mice (Wang et al., 2021).

Taken together, our and other findings suggest that the detection and reaction to ethologically relevant moving visual stimuli, such as a bird of prey or a vehicle, is implemented by a division of labor among OFF-GC classes. sOFF generate AP firing in

response to the local motion of visual features, driven by the engagement of active dendritic integration. A mechanism that enables sensitivity to moving visual stimuli across a wide speed and contrast range, which is engaged at the stimulus's leading edge but suppressed by global motion of the visual world. Moreover, our results demonstrate that active dendritic integration allows sOFF-GCs tiled across retinal space to generate an unbroken representation of such stimuli as they move through visual space. We suggest that these characteristics are likely to be important for the detection of avian predators by the rabbit, leading to the initiation of escape behavior (Kane et al., 2015). In contrast, because of passive dendritic integration properties, sensitivity of tOFF-GCs to small sized moving visual stimuli is reduced, and hence, tOFF-GCs are ill-suited for the detection of predators but instead are well-tuned to signal the close approach and final attack of a predator (Figure S4; Wang et al., 2021). Parenthetically, the ideal flight plan of avian predators has been found to be one where relative motion is minimized, by the matching of pursuit speed with the speed of the fleeing rabbit, and the positioning of final attack to the blind spot of rabbits, a narrow area of space behind the animals' head (Kane et al., 2015). Thus, the cell-class-specific expression of active dendritic integration in OFF-GCs in the rabbit retina forms computations essential for animal survival.

STAR★METHODS

Detailed methods are provided in the online version of this paper and include the following:

- **KEY RESOURCES TABLE**
- **RESOURCE AVAILABILITY**
 - Lead contact
 - Materials availability
 - Data and code availability
- **EXPERIMENTAL MODEL AND SUBJECT DETAILS**
 - Animals
- **METHOD DETAILS**
 - Retinal preparation
 - Electrophysiological recording
 - Visual stimulation and analysis
 - Computer simulation
 - Morphological reconstruction and immunohistochemistry
 - Experimental design
- **QUANTIFICATION AND STATISTICAL ANALYSIS**

SUPPLEMENTAL INFORMATION

Supplemental information can be found online at <https://doi.org/10.1016/j.neuron.2022.06.009>.

ACKNOWLEDGMENTS

We are grateful to Dr. Lee Fletcher, Dr. Ben Sivyer, and Rowan Tweedale for comments on an earlier draft of the manuscript and Prof. Mandyam Srinivasan for advice. This work was supported by the National Health and Medical Research Council of Australia (GNT1082257 and GA59869 to S.R.W.). Imaging was performed at the Queensland Brain Institute's Advanced Microscopy

Facility, generously supported by the Australian Government through the Australian Research Council LIEF grants LE100100074 and LE130100078.

AUTHOR CONTRIBUTIONS

Experimental: A.B. performed experiments. Analysis: A.B., X.Z., and S.R.W. analyzed electrophysiological data and performed modeling. A.B. and X.Z. performed immunohistochemistry, confocal imaging, and neuronal reconstructions. Conceptualization: S.R.W. Writing: S.R.W. wrote the original draft manuscript, all authors participated in writing, reviewing, and editing of the manuscript.

DECLARATION OF INTERESTS

The authors declare no competing interests.

Received: February 8, 2022

Revised: April 27, 2022

Accepted: June 7, 2022

Published: July 7, 2022

REFERENCES

Awaramani, G.B., and Slaughter, M.M. (2000). Origin of transient and sustained responses in ganglion cells of the retina. *J. Neurosci.* 20, 7087–7095. <https://doi.org/10.1523/jneurosci.20-18-07087.2000>.

Baden, T., Berens, P., Franke, K., Román Rosón, M., Bethge, M., and Euler, T. (2016). The functional diversity of retinal ganglion cells in the mouse. *Nature* 529, 345–350. <https://doi.org/10.1038/nature16468>.

Beaudoin, D.L., Kupershmidt, M., and Demb, J.B. (2019). Selective synaptic connections in the retinal pathway for night vision. *J. Comp. Neurol.* 527, 117–132. <https://doi.org/10.1002/cne.24313>.

Beaulieu-Laroche, L., Toloza, E.H.S., Brown, N.J., and Harnett, M.T. (2019). Widespread and highly correlated somato-dendritic activity in cortical layer 5 neurons. *Neuron* 103, 235–241.e4. <https://doi.org/10.1016/j.neuron.2019.05.014>.

Berry, M.J., 2nd, Brivanlou, I.H., Jordan, T.A., and Meister, M. (1999). Anticipation of moving stimuli by the retina. *Nature* 398, 334–338. <https://doi.org/10.1038/18678>.

Bittner, K.C., Grienberger, C., Vaidya, S.P., Milstein, A.D., Macklin, J.J., Suh, J., Tonegawa, S., and Magee, J.C. (2015). Conjunctive input processing drives feature selectivity in hippocampal CA1 neurons. *Nat. Neurosci.* 18, 1133–1142. <https://doi.org/10.1038/nn.4062>.

Brombas, A., Kalita-de Croft, S., Cooper-Williams, E.J., and Williams, S.R. (2017). Dendro-dendritic cholinergic excitation controls dendritic spike initiation in retinal ganglion cells. *Nat. Commun.* 8, 15683. <https://doi.org/10.1038/ncomms15683>.

Brown, S.P., He, S., and Masland, R.H. (2000). Receptive field microstructure and dendritic geometry of retinal ganglion cells. *Neuron* 27, 371–383. [https://doi.org/10.1016/s0896-6273\(00\)00044-1](https://doi.org/10.1016/s0896-6273(00)00044-1).

Buldyrev, I., and Taylor, W.R. (2013). Inhibitory mechanisms that generate centre and surround properties in ON and OFF brisk-sustained ganglion cells in the rabbit retina. *J. Physiol.* 591, 303–325. <https://doi.org/10.1113/jphysiol.2012.243113>.

Cembrowski, M.S., and Spruston, N. (2019). Heterogeneity within classical cell types is the rule: lessons from hippocampal pyramidal neurons. *Nat. Rev. Neurosci.* 20, 193–204. <https://doi.org/10.1038/s41583-019-0125-5>.

DeVries, S.H. (1999). Correlated firing in rabbit retinal ganglion cells. *J. Neurophysiol.* 81, 908–920. <https://doi.org/10.1152/jn.1999.81.2.908>.

Doron, G., Shin, J.N., Takahashi, N., Drüke, M., Bocklisch, C., Skenderi, S., de Mont, L., Toumazou, M., Ledderose, J., Brecht, M., et al. (2020). Perirhinal input to neocortical layer 1 controls learning. *Science* 370, eaaz3136. <https://doi.org/10.1126/science.aaz3136>.

Farrow, K., Teixeira, M., Szikra, T., Viney, T.J., Balint, K., Yonehara, K., and Roska, B. (2013). Ambient illumination toggles a neuronal circuit switch in the retina and visual perception at cone threshold. *Neuron* 78, 325–338. <https://doi.org/10.1016/j.neuron.2013.02.014>.

Fletcher, L.N., and Williams, S.R. (2019). Neocortical topology governs the dendritic integrative capacity of layer 5 pyramidal neurons. *Neuron* 101, 76–90.e4. <https://doi.org/10.1016/j.neuron.2018.10.048>.

Hughes, A. (1972). A schematic eye for the rabbit. *Vision Res.* 12, 123–138. [https://doi.org/10.1016/0042-6989\(72\)90143-5](https://doi.org/10.1016/0042-6989(72)90143-5).

Jain, V., Murphy-Baum, B.L., deRosenroll, G., Sethuramanujam, S., Delsey, M., Delaney, K.R., and Awaramani, G.B. (2020). The functional organization of excitation and inhibition in the dendrites of mouse direction-selective ganglion cells. *eLife* 9, e52949. <https://doi.org/10.7554/elife.52949>.

Kane, S.A., Fulton, A.H., and Rosenthal, L.J. (2015). When hawks attack: animal-borne video studies of goshawk pursuit and prey-evasion strategies. *J. Exp. Biol.* 218, 212–222. <https://doi.org/10.1242/jeb.108597>.

Koch, C., Poggio, T., and Torre, V. (1983). Nonlinear interactions in a dendritic tree: localization, timing, and role in information processing. *Proc. Natl. Acad. Sci. USA* 80, 2799–2802. <https://doi.org/10.1073/pnas.80.9.2799>.

Lavzin, M., Rapoport, S., Polksky, A., Garion, L., and Schiller, J. (2012). Nonlinear dendritic processing determines angular tuning of barrel cortex neurons *in vivo*. *Nature* 490, 397–401. <https://doi.org/10.1038/nature11451>.

London, M., and Häusser, M. (2005). Dendritic computation. *Annu. Rev. Neurosci.* 28, 503–532. <https://doi.org/10.1146/annurev.neuro.28.061604.135703>.

Malik, R., Dougherty, K.A., Parikh, K., Byrne, C., and Johnston, D. (2016). Mapping the electrophysiological and morphological properties of CA1 pyramidal neurons along the longitudinal hippocampal axis. *Hippocampus* 26, 341–361. <https://doi.org/10.1002/hipo.22526>.

Moore, J.J., Ravassard, P.M., Ho, D., Acharya, L., Kees, A.L., Vuong, C., and Mehta, M.R. (2017). Dynamics of cortical dendritic membrane potential and spikes in freely behaving rats. *Science* 355, eaaj1497. <https://doi.org/10.1126/science.aaj1497>.

Münch, T.A., da Silveira, R.A., Siegert, S., Viney, T.J., Awaramani, G.B., and Roska, B. (2009). Approach sensitivity in the retina processed by a multifunctional neural circuit. *Nat. Neurosci.* 12, 1308–1316. <https://doi.org/10.1038/nn.2389>.

Oesch, N., Euler, T., and Taylor, W.R. (2005). Direction-selective dendritic action potentials in rabbit retina. *Neuron* 47, 739–750. <https://doi.org/10.1016/j.neuron.2005.06.036>.

Olveczky, B.P., Baccus, S.A., and Meister, M. (2003). Segregation of object and background motion in the retina. *Nature* 423, 401–408. <https://doi.org/10.1038/nature01652>.

Pastoll, H., Garden, D.L., Papastathopoulos, I., Sürmeli, G., and Nolan, M.F. (2020). Inter- and intra-animal variation in the integrative properties of stellate cells in the medial entorhinal cortex. *eLife* 9, e52258. <https://doi.org/10.7554/elife.52258>.

Peichl, L. (1991). Alpha ganglion cells in mammalian retinae: common properties, species differences, and some comments on other ganglion cells. *Vis. Neurosci.* 7, 155–169. <https://doi.org/10.1017/s0952523800011020>.

Poleg-Polsky, A., and Diamond, J.S. (2016). NMDA receptors multiplicatively scale visual signals and enhance directional motion discrimination in retinal ganglion cells. *Neuron* 89, 1277–1290. <https://doi.org/10.1016/j.neuron.2016.02.013>.

Rall, W. (1967). Distinguishing theoretical synaptic potentials computed for different soma-dendritic distributions of synaptic input. *J. Neurophysiol.* 30, 1138–1168. <https://doi.org/10.1152/jn.1967.30.5.1138>.

Ran, Y., Huang, Z., Baden, T., Schubert, T., Baayen, H., Berens, P., Franke, K., and Euler, T. (2020). Type-specific dendritic integration in mouse retinal ganglion cells. *Nat. Commun.* 11, 2101. <https://doi.org/10.1038/s41467-020-15867-9>.

Rolotti, S.V., Blockus, H., Sparks, F.T., Priestley, J.B., and Losonczy, A. (2022). Reorganization of CA1 dendritic dynamics by hippocampal sharp-wave ripples during learning. *Neuron* 110, 977–991.e4. <https://doi.org/10.1016/j.neuron.2021.12.017>.

Sanes, J.R., and Masland, R.H. (2015). The types of retinal ganglion cells: current status and implications for neuronal classification. *Annu. Rev. Neurosci.* 36, 221–246. <https://doi.org/10.1146/annurev-neuro-071714-034120>.

Schachter, M.J., Oesch, N., Smith, R.G., and Taylor, W.R. (2010). Dendritic spikes amplify the synaptic signal to enhance detection of motion in a simulation of the direction-selective ganglion cell. *PLoS Comput. Biol.* 6. <https://doi.org/10.1371/journal.pcbi.1000899>.

Schmidt-Hieber, C., Toleikyte, G., Aitchison, L., Roth, A., Clark, B.A., Branco, T., and Häusser, M. (2017). Active dendritic integration as a mechanism for robust and precise grid cell firing. *Nat. Neurosci.* 20, 1114–1121. <https://doi.org/10.1038/nn.4582>.

Schwartz, G.W., Okawa, H., Dunn, F.A., Morgan, J.L., Kerschensteiner, D., Wong, R.O., and Rieke, F. (2012). The spatial structure of a nonlinear receptive field. *Nat. Neurosci.* 15, 1572–1580. <https://doi.org/10.1038/nn.3225>.

Sheffield, M.E., and Dombeck, D.A. (2015). Calcium transient prevalence across the dendritic arbor predicts place field properties. *Nature* 517, 200–204. <https://doi.org/10.1038/nature13871>.

Sivyer, B., and Williams, S.R. (2013). Direction selectivity is computed by active dendritic integration in retinal ganglion cells. *Nat. Neurosci.* 16, 1848–1856. <https://doi.org/10.1038/nn.3565>.

Smith, S.L., Smith, I.T., Branco, T., and Häusser, M. (2013). Dendritic spikes enhance stimulus selectivity in cortical neurons *in vivo*. *Nature* 503, 115–120. <https://doi.org/10.1038/nature12600>.

Soltesz, I., and Losonczy, A. (2018). CA1 pyramidal cell diversity enabling parallel information processing in the hippocampus. *Nat. Neurosci.* 21, 484–493. <https://doi.org/10.1038/s41593-018-0118-0>.

Stuart, G.J., and Spruston, N. (2015). Dendritic integration: 60 years of progress. *Nat. Neurosci.* 18, 1713–1721. <https://doi.org/10.1038/nn.4157>.

Takahashi, N., Oertner, T.G., Hegemann, P., and Larkum, M.E. (2016). Active cortical dendrites modulate perception. *Science* 354, 1587–1590. <https://doi.org/10.1126/science.aah6066>.

Trenholm, S., McLaughlin, A.J., Schwab, D.J., Turner, M.H., Smith, R.G., Rieke, F., and Awatramani, G.B. (2014). Nonlinear dendritic integration of electrical and chemical synaptic inputs drives fine-scale correlations. *Nat. Neurosci.* 17, 1759–1766. <https://doi.org/10.1038/nn.3851>.

Vaney, D.I., Sivyer, B., and Taylor, W.R. (2012). Direction selectivity in the retina: symmetry and asymmetry in structure and function. *Nat. Rev. Neurosci.* 13, 194–208. <https://doi.org/10.1038/nrn3165>.

Velte, T.J., and Masland, R.H. (1999). Action potentials in the dendrites of retinal ganglion cells. *J. Neurophysiol.* 81, 1412–1417. <https://doi.org/10.1152/jn.1999.81.3.1412>.

Völgyi, B., Pan, F., Paul, D.L., Wang, J.T., Huberman, A.D., and Bloomfield, S.A. (2013). Gap junctions are essential for generating the correlated spike activity of neighboring retinal ganglion cells. *PLoS One* 8, e69426. <https://doi.org/10.1371/journal.pone.0069426>.

Wang, F., Li, E., De, L., Wu, Q., and Zhang, Y. (2021). OFF-transient alpha RGCs mediate looming triggered innate defensive response. *Curr. Biol.* 31, 2263–2273.e3. <https://doi.org/10.1016/j.cub.2021.03.025>.

Wässle, H., Peichl, L., and Boycott, B.B. (1981). Morphology and topography of on- and off-alpha cells in the cat retina. *Proc. R. Soc. Lond. B Biol. Sci.* 212, 157–175. <https://doi.org/10.1098/rspb.1981.0032>.

Williams, S.R., and Stuart, G.J. (2002). Dependence of EPSP efficacy on synapse location in neocortical pyramidal neurons. *Science* 295, 1907–1910. <https://doi.org/10.1126/science.1067903>.

Williams, S.R., and Stuart, G.J. (2003). Role of dendritic synapse location in the control of action potential output. *Trends Neurosci.* 26, 147–154. [https://doi.org/10.1016/S0166-2236\(03\)00035-3](https://doi.org/10.1016/S0166-2236(03)00035-3).

Xu, N.L., Harnett, M.T., Williams, S.R., Huber, D., O'Connor, D.H., Svoboda, K., and Magee, J.C. (2012). Nonlinear dendritic integration of sensory and motor input during an active sensing task. *Nature* 492, 247–251. <https://doi.org/10.1038/nature11601>.

STAR★METHODS

KEY RESOURCES TABLE

REAGENT or RESOURCE	SOURCE	IDENTIFIER
Antibodies		
Goat polyclonal anti-ChAT	Millipore	Cat# AB144P
Donkey anti-goat Alexa Fluor Plus 488	Thermo Fisher Scientific	Cat# A32814
Chemicals, peptides, and recombinant proteins		
Streptavidin-Alexa Fluor 594	Thermo Fisher Scientific	Cat# S11227
TTX	Alomone	CAS: 18660-81-6
Biocytin	Sigma	CAS: 576-19-2
Ames Medium	Sigma	Cat# A1420-10X1L
Aqua Polymount	Polysciences Inc.	Cat# 08381
Experimental models: Organisms/strains		
New Zealand white rabbits	Flinders University, Australia	N/A
Software and algorithms		
Axograph X (1.6.4)	Axograph	N/A
Prism (9)	Graphpad	N/A
SigmaPlot (12 & 13)	SysStat Software	N/A
Office 365	Microsoft	N/A
Neurolucida	MicroBrightField	N/A
Neurolucida Explorer	MicroBrightField	N/A
Fiji/ImageJ	http://fiji.sc/	N/A
Zen 2008	Zeiss	N/A
Python (3.8.8)	Python Software Foundation	https://www.python.org/
Igor Pro	Wavemetrics	N/A
Visual stimuli software	Taylor Lab, Berkeley University of California Smith Lab, University of Pennsylvania	N/A
Bipolar cell array algorithm	https://github.com/WilliamsLab-GitHub/Bipolar_Simulation	https://doi.org/10.5281/zenodo.6601962
Dendritic perimeter algorithm	https://github.com/WilliamsLab-GitHub/Bipolar_Simulation	https://doi.org/10.5281/zenodo.6601962
Zen 2008	Zeiss	N/A
Other		
Edge GS 1X20 (Night Vision goggles)	Extravision Australia PTY LTD	Cat# YU75095
DSVGA Monochrome White OLED_XL	eMagin	Cat# EMA-101126-01
Long Range Infrared Spotlight	Jaycar Australia	Cat# QC3654

RESOURCE AVAILABILITY

Lead contact

Further information and requests for resources and reagents should be directed to and will be fulfilled by the lead contact, Stephen Williams (srw@uq.edu.au).

Materials availability

This study did not generate any unique reagents.

Data and code availability

All data reported in this paper will be shared by the **lead contact** upon request. All original code has been deposited at (https://github.com/WilliamsLab-GitHub/Bipolar_Simulation) and is publicly available as of the date of publications. DOIs are listed in the **key resources table**. Any additional information required to reanalyze the data reported in this paper is available from the **lead contact** on request.

EXPERIMENTAL MODEL AND SUBJECT DETAILS

Animals

New Zealand white rabbits were obtained from the Flinders University breeding colony. Rabbits were housed in groups of five in pens, and subject to a 12 h light/dark cycle, food and water were available *ad libitum*. Female and male adult rabbits (age= 83 ± 2 days, range= 47 to 156 days; female= 31, male= 77) were used. We did not note any sex specific differences in the distribution of the OFF-GC classes reported (ratio of the number of recorded tOFF and sOFF-GCs: female= 1.42, male= 1.68).

METHOD DETAILS

Retinal preparation

All experiments were approved by the Animal Ethics Committee of The University of Queensland in accordance with the Australian Code of Practice for the Care and Use of Animals for Scientific Purposes. Rabbits were dark-adapted for 1-2 h, anesthetized with ketamine (12 mg / kg of body weight, intramuscular) and xylazil (12 mg / kg, intramuscular) then overdosed with pentobarbarbitone sodium (150 mg / kg, intravenous), before the eyes were quickly enucleated, hemisected, and placed in carbogenated Ames solution (8.8 g / L Ames, 1.9 g / L sodium bicarbonate, 0.75 g / L glucose) at room temperature. Large sections of the ventral peripheral retina were separated from the sclera and pigmented epithelial layer and stored in carbogenated Ames solution at room temperature (22 - 24°C). All procedures were carried out under infrared illumination, with the aid of night-vision goggles (Pulsar Edge GS 1x20). A single section was placed in a recording chamber perfused with Ames solution at 35 - 37°C.

Electrophysiological recording

Whole-cell recordings were made from visually targeted OFF-GCs using infrared differential interference contrast video microscopy based on depth in the ganglion cell layer, soma size and shape, and characteristic patterns of dendritic arborization within the inner plexiform layer. Somatic or simultaneous somato-dendritic whole-cell recordings were made with identical current-clamp amplifiers configured in “bridge-mode” (BVC 700A, Dagan Corporation). Voltage and current signals were low-pass filtered at dc to 10 kHz and sampled at 50 kHz. Whole-cell recording pipettes were filled with (in mM): 135 K-gluconate; 7 NaCl; 10 HEPES; 10 phosphocreatine; 2 Na₂-ATP; 0.3 Na-GTP; 2 MgCl₂ and 0.35 Alexa Fluor 594 (Molecular Probes) (pH 7.3-7.4; KOH), and had an open tip resistance of 4 - 5 MΩ for somatic and 15 - 20 MΩ for dendritic pipettes. In some experiments, the pipette solution included 0.5 % biocytin (wt / vol, 5 mg / ml). Cell-attached voltage-clamp recordings ($V_H = 0$ mV) were made from dendritic sites, using electrodes filled with the above pipette solution. No correction was made for liquid junction potential. In some experiments a third, independently manipulated pipette with characteristics similar to those used for somatic recordings was used to locally pressure apply tetrodotoxin (3 μM dissolved in Ames solution, duration= 5 to 10 s) to the region of a small hole torn in the inner limiting membrane at a site aligned with the dendritic recording (Sivyer and Williams, 2013). At the termination of each whole-cell recording, the location of the recording pipettes and neuronal morphology were examined by fluorescence microscopy and recorded using a digital camera (QImaging).

Visual stimulation and analysis

Visual stimuli were generated using custom software (developed by W. R. Taylor (Oregon Health and Science University) and R. G. Smith (University of Pennsylvania)), and presented on a 800 × 600 pixel OLED screen (eMagin). Images were projected and focussed on the plane of photoreceptor outer segments to physiologically activate the retinal network through the microscope substage condenser. The background illumination was standardly set to a level ≈ 3.6 × 10¹¹ quanta / cm² / s and dark stimuli were delivered as areas of decreased luminance, expressed as a percentage below the level of background illumination (range= 10 to 100%). In some experiments the background was changed over a range 1.3 × 10⁹ quanta / cm² / s to 1.2 × 10¹³ quanta / cm² / s. In each recorded OFF-GC the action potential (AP) firing pattern evoked in response to flashed dark spot stimuli, centred at the soma of the recorded GC, was used to determine GC class (size= 200 - 500 μm, duration= 0.5 s, inter trial interval= 7.5 s). In addition, a range of flashed (0.5 s) dark spot stimuli (50 - 500 μm) projected at determined receptive field loci were employed. The receptive fields of OFF-GCs were also mapped by the presentation of flashed (0.5 s, inter-trial interval= 5 s) dark square stimuli (50 μm, sustained; 100 μm, transient) at pseudo-randomly determined positions within a 800 μm by 800 μm matrix (sustained) or 1400 μm by 1400 μm matrix (transient) centred at the soma of the recorded GC. Dark bars (height= 500 to 1000 μm, width= 5 to 500 μm) were flashed or moved across retinal space over a wide speed range (0.5 to 7 mm/s) (inter-trial interval= 7.5 s). The direction selectivity of OFF-GCs was investigated by the presentation of dark bars moved in 1 of 12 directions at 30° intervals, and output responses were represented as Rayleigh plots. The motion sensitivity of OFF-GCs was also investigated by the presentation of moving grating stimuli, composed of alternating dark and light bands with widths of 250 μm that moved with a speed of 0.5 mm/s for a period of 6 s (inter-trial interval= 12 s). Moving gratings were either spatially confined (500 μm diameter), or uniformly presented over a wide projection area (2 by 2 mm) centred at the soma of the recorded GC. All electrophysiological data were analysed in Axograph X. APs and spikelets were detected using the derivative detection algorithm of Axograph X, with a threshold of 5 V.s⁻¹, and manually validated. The rise-time of events was measured at 10-90 %, and half-width at 50% of the full amplitude. Heat maps of AP firing, and dendritic geometry were constructed in SigmaPlot (version 14). The time of onset of dendritic synaptic depolarization was calculated from digital averages of consecutive trials (n= 5 - 10), by fitting a linear regression to the rising slope of the evoked response and extrapolating to a time when the function reached the resting potential.

Computer simulation

A simulated mosaic of bipolar cell axonal footprints was generated using poisson disk sampling to produce a series of unique random disk arrays ($n=200$). The size of each disc (diameter= 40 μm), the density (522 discs / mm^2) and the spatial coverage (0.66) of each array were in accordance with anatomical descriptions of the mosaic of bipolar cell axonal footprints in the rabbit, and previous simulations (Brown et al., 2000; Schwartz et al., 2012). We positioned the reconstructed dendritic tree of experimentally recorded OFF-GCs into the centre of these arrays. As bipolar cells are thought to make synaptic contact with the dendrites of GCs which overlay their axonal fields (Sanes and Masland, 2015), we counted the number of discs that were overlaid by dendritic segments, within the perimeter of the dendritic tree of reconstructed neurons. The perimeter of the dendritic tree was described by an algorithm which slid a 30°, soma-centred search sector, at 10° intervals, around the reconstruction, to describe distal dendritic points. These points were joined to form the perimeter. Disc coverage was determined by dividing the number of discs enclosed by the perimeter of the dendritic tree, by those which overlaid dendritic segments. All simulation code was written in Anaconda (4.10.1) and is publicly available (https://github.com/WilliamsLab-GitHub/Bipolar_Simulation).

Morphological reconstruction and immunohistochemistry

Cells filled with biocytin were fixed (4 % paraformaldehyde in phosphate buffered saline (PBS), pH 7.3-7.4, 1-2 h), washed in PBS (3 x 10 min), pre-incubated with donkey serum (2%), Triton X-100 (0.3 %) in PBS, then reacted with a primary antibody targeting choline acetyltransferase (goat anti-ChAT-AB144P, Millipore, 1:500) in 2% donkey serum, 0.3 % Triton X-100, 0.05% sodium azide in PBS for 3-5 days at room temperature with shaking. They were then washed in PBS (3 x 10 min) and reacted with secondary antibody conjugated to Alexa Fluor Plus 488 (donkey anti-goat Alexa Fluor Plus 488, 1:500, ThermoFisher Scientific A32814), 0.1% streptavidin conjugated with Alexa Fluor 594 (Invitrogen), 0.3% Triton x-100, 0.05% sodium azide in PBS overnight at room temperature, after which they were washed (PBS, 3 x 10 min) and mounted in Aqua Polymount (Polysciences Inc.). Mounted retina were imaged on a Zeiss LSM510, AxioObserver confocal microscope using a 63x (Plan-Aprochromat 1.4 NA) oil objective. Photomicrographs were obtained at a resolution of 2048 x 2048 and a Z-step size of 0.37 μm . Images were analysed with ImageJ. OFF-GCs were manually reconstructed with Neurolucida (MicroBrightField) at high digital magnification and the reconstructions were visualized and analysed with Neurolucida Explorer (MicroBrightField) and Excel (Microsoft).

Experimental design

No strategy for randomization and/or stratification was adopted. It was not possible to perform this study blinded. Inclusion and exclusion criteria for individual data types are detailed below.

QUANTIFICATION AND STATISTICAL ANALYSIS

Values reported are mean \pm standard error of the mean (SEM), and n values represent the number of cells (individual n values are shown in the results section and in the Figure Legends). Statistical significance was defined as when the probability of the data being observed under a null hypothesis was less than an alpha level of 0.05. The normality of the distribution of data was tested using a combination of Anderson-Darling, D'Agostino and Pearson, and the Shapiro-Wilk tests. Significance was tested with a two-tail Students' t-test, ANOVA, or the Mann-Whitney test. Welch's correction was used for samples with unequal variance. Details of statistical tests can be found in the results section. Statistical analysis was carried out using Prism 9 (Graphpad). Electrophysiological data were excluded in instances when the membrane potential, or access resistance were unstable, or if cells exhibited a high spontaneous AP firing rate relative to the norm.